

Numerical Simulation of Gas Jet Effects in Laser Machining

Kai Chen, Y. Lawrence Yao, and Vijay Modi
Department of Mechanical Engineering
Columbia University
New York, NY 10027

Abstract

In this paper, the interaction of a transonic, turbulent axisymmetric jet with the workpiece is studied. Numerical simulations are carried out using an explicit, coupled solution algorithm with solution-based mesh adaptation. Effect of gas pressure and nozzle standoff distance on structure of the supersonic shock pattern is studied. Experiments are carried out to study the effect of processing parameters such as gas pressure and standoff distance. The measured results match and hence validate the simulations. The interaction of the oblique incident shock with the normal standoff shock is found to contribute to a significant reduction in the total pressure at the machining front when the nozzle pressure increases beyond a certain point. The associated reduction in flow rate, fluctuations of pressure gradient and shear force at the machining front could lower the material removal capability of the gas jet and possibly result in a poorer surface finish.

Nomenclature

A	area of delivery nozzle exit	A_m	area of measurement nozzle exit
c_D	nozzle discharge coefficient	d	hole diameter
D	nozzle exit diameter	H	standoff distance
\dot{m}	mass flow rate	M	Mach number
p	static pressure	p_t	total pressure
P_e	total gauge pressure at nozzle exit	R	universal gas constant
T	temperature	T_0	stagnation temperature
V_m	velocity at measurement nozzle exit	ρ	density
ρ_m	density at measurement nozzle exit	γ	specific heat ratio
subscripts for \dot{m}			
n	delivery nozzle	m	measurement nozzle
h	hole		

1. Introduction

The assist gas plays an important role in laser machining. It provides a mechanical force to eject the melt from the cut zone and cools the cut zone by forced convection. Inefficient removal of the molten layer can lead to a deterioration in cut surface. The role of oxygen pressure in laser cutting of steels was studied experimentally by Ivarson *et al.* [1]. They found that there are two optimum pressure ranges where the cut quality is good. Numerical calculations of the three-dimensional turbulent oxygen jet by O'Neill and Steen [2] showed that entrainment of impurities occurs inside the cut kerf and this can have detrimental effects on oxidation and cutting capability.

The use of an off-axis nozzle in tandem with a coaxial nozzle was investigated by Chryssolouris and Choi [3], and the use of a single off-axis nozzle was studied experimentally by Brandt and Settles [4]. Other supersonic nozzle configurations have also been considered to improve the effects of gas jet [5, 6]. A comprehensive review of the gas jet effects was presented by Fieret *et al* [7], in which a Mach shock was found to reduce the stagnation pressure at the workpiece.

In industrial practice, nozzles are positioned close to the workpiece and nozzle pressures are chosen within a certain range for laser machining. There is however little theoretical work to systematically study the effects of a gas jet and process parameters such as nozzle position and gas pressure. For a convergent nozzle, the flow downstream of the nozzle exit becomes supersonic if the upstream total reservoir pressure is greater than 1.89 bar, a condition common to laser machining. Downstream of the nozzle exit, oblique shock cells are formed. Experimental and analytical studies have examined the shock behavior of free jets and impingement jets. At underexpansion ratios below 3 to 4 pressure equilibrium is achieved through a series of repetitive oblique shock cells, which eventually decay into a conventional constant-pressure jet (Figure 1-a). For underexpansion ratios greater than 3-4 however, the first shock cells contain normal shock waves or a Mach disk [8]. The normal impingement of a underexpanded jet onto a flat plate located within the first few shock cells leads to the formation of a well-defined standoff shock upstream off the plate. Across the standoff shock, the jet suddenly decelerates to subsonic flow and is then deflected by the plate [9] (see Figure 1-b). Since most laser machining operates at a total pressure between 3 to 5 bar, i.e. in the range of moderately underexpanded jets to the onset of highly underexpanded jet, the above descriptions are helpful in understanding the flow structure present in laser machining. The current effort aims at examining the gas jet effects by carrying out numerical simulations and experiments for a geometry that closely mimics the real machining case.

2. Numerical Simulations

In order to make the problem amenable to analysis while addressing the main issues of the study, the following assumptions are made:

A conical convergent nozzle is assumed to deliver a gas jet that normally impinges onto a workpiece plate with a through hole concentric with the nozzle (Figure 2). The through hole diameter d is assumed to be smaller than the exit diameter of nozzle D . The assumption of a through hole that is concentric with the nozzle makes the problem axisymmetric, thus reducing the dimensionality of the problem. Axisymmetric studies have significance not only because they corresponds to the laser drilling case, but because they also reveal the generic behavior of the gas flow upstream of the machining front. This flow behavior is expected to be relatively independent of the actual cut geometry. The thermal interactions of the laser and the possibly reactive gas with workpiece material including melting and vaporization are not considered.

The flow solver is an unstructured finite-volume code with the capability of adaptive grid refinement. The solver uses a semi-discrete finite-volume formulation, resulting in a consistent approximation to the conservation laws in integral form. Nonequilibrium wall functions are used for near wall treatment in conjunction with the RNG turbulence model. Since the delivery nozzle is a convergent type and the flow at the nozzle exit is always choked for pressures of interest, our computational domain boundary is located at the nozzle exit plane. The flow at the nozzle exit is

assumed to be uniform and at sonic conditions. Whereas this may cause some inaccuracies particularly close to the nozzle lip, it will not influence the flow characteristic downstream. Sonic conditions are enforced at the nozzle lip by specifying the total pressure and total temperature according to one-dimensional isentropic flow relations:

$$\frac{p_0}{p} = \left[1 + \frac{\gamma - 1}{2} M^2 \right]^{\frac{\gamma}{\gamma - 1}}, \quad (1)$$

$$\frac{T_0}{T} = 1 + \frac{\gamma - 1}{2} M^2, \quad (2)$$

where the Mach number M is set to unity. At inlet boundaries the total pressure, static pressure, total temperature and the flow direction are imposed. At the subsonic outlet boundary, the static pressure is specified whereas the remaining flow properties are extrapolated. No-slip wall and symmetry boundary conditions are applied at the plate and the centerline respectively.

3. Experimental Setup

The experimental setup (Figure 3) was designed to measure the mass flow rate through a predrilled hole in the workpiece with variation of total nozzle pressure and standoff distance. While the mass flow rate through the cut kerf may not be of concern in itself for laser machining, it is directly related to the total pressure at the machining front which in turn is an important factor in determining the material removal capability of the gas jet. The measurement of the mass flow rate also provides a convenient and viable verification of the simulation results.

A commercial sonic (converging-only) nozzle with a nozzle diameter $D = 1.35\text{mm}$ is used. Compressed air from a gas tank is fed into the nozzle through a gas inlet where a pressure gauge was set. The gas exiting the nozzle impinges on an plate (or workpiece) with a predrilled hole in it. The impingement plate is 1.5mm thick with through a hole of 0.711mm in diameter. The nozzle flow \dot{m}_n is in part deflected by the plate. The remaining flow, through hole flow \dot{m}_h enters the hole. The small hole diameter and the high gas speeds make it difficult to measure the through flow directly. Hence a collection box is placed underneath to collect the flow and direct it to a 10mm measurement nozzle at considerably lower flow speed. A micrometer is used to obtain a precise measurement of the stand-off distance. The velocity of the gas leaving the measurement nozzle (V_m) is then measured using a hot-film anemometer (TSI 8350). The measurement nozzle contour guarantees that the velocity profile of the gas steam is nearly uniform. The mass flow rate through the measurement nozzle ($\rho_m A_m V_m$) and hence the through hole flow \dot{m}_h is obtained.

The hot-film anemometer was calibrated using a pitot tube in the 40mmx230mm test section of a wind tunnel. A least square linear fitting was used to obtain the numerical values for the velocities read from the hot-film velocimeter. Since the flow at the throat of the delivery nozzle is always choked, it is possible to relate the upstream total pressure p_t to the mass flow rate from nozzle \dot{m}_n . The following relationship holds at the sonic nozzle exit

$$\dot{m}_n = c_D A p_t \left[\left(\frac{2}{RT} \right) \left(\frac{\gamma}{\gamma + 1} \right) \left(\frac{2}{\gamma + 1} \right)^{\frac{2}{\gamma - 1}} \right]^{\frac{1}{2}}. \quad (3)$$

The total pressure P_e thus can be obtained by knowing the mass flow rate from the sonic nozzle. In the above relationship, the mass flow rate is corrected for viscous losses using a nozzle discharge coefficient c_D . The same experimental apparatus was used to measure the mass flow rate from the sonic nozzle at zero standoff. The collection box however was raised to let the delivery nozzle lip stick into the box and the gap was sealed to prevent leakage. Thus the mass flow rate from the sonic nozzle can be obtained in the same manner as described before.

4. Results and Discussions

Flow behavior within the hole as well as \dot{m}_h are essentially determined by the total gas pressure immediately upstream of the hole. This pressure is nearly equal to the total pressure downstream of the normal standoff shock. It is desirable to minimize the total pressure loss through the normal shock. This can be achieved by changing the shock structure, as will be shown by the experimental and simulation results.

Two sets of measurements were carried. For Group 1 experiments, the total gauge pressure at nozzle exit P_e was varied continuously between 120 kPa and 490 kPa for standoff distance $H = 1.0$ and 2.0 mm. For Group 2 experiments however, two distinct values of P_e were chosen and H was varied continuously from 0 to 3.5mm. The above described conditions are summarized in the following table:

	d (mm)	H (mm)		P_e (kPa)	
Group 1	0.711	1.0	2.0	Varied From 120 to 490	
Group 2	0.711	Varied From 0 to 3.5		125	363

The measured \dot{m}_h data are shown in Figure 4 for Group 1 experiments together with the simulation results. The simulations were carried out over the computational domain shown in Figure 2 for the same operating pressure conditions as the experiments. For $H = 1.0$ mm, \dot{m}_h is found to monotonically and linearly increase with P_e . For $H = 2.0$ mm however, \dot{m}_h first increases with total pressure until it reaches a local maximum around $P_e = 240$ kPa. The mass flow rate then reduces even as total pressure increases, until it reaches a local minimum and begins to increase again. Since one would expect \dot{m}_h to monotonically increase with P_e , the unusual behavior for $H = 2.0$ mm may indicate a change in shock structure which can have a significant effect on flow behavior. The computed results follow the trends in the experimental results closely and capture the local maximum/minimum in \dot{m}_h for $H = 2$ mm. The experimental uncertainties in the measurements are shown as error bars in the figure.

To further understand the interesting phenomena seen in Figure 4, contours of static pressure at two different nozzle pressure levels for $H = 2$ mm are shown in Figures 5-a and b. The objective of Figure 5 is to reveal the changes in shock structure for $P_e = 207$ kPa (to the left of the local maximum) and $P_e = 276$ kPa (to the right of the local maximum) shown in Figure 4. At the lower P_e of 207 kPa in Figure 5-a, the oblique shock has a larger deflection angle as expected from the theory of oblique shock waves. The incident shock waves meet at the centerline and are reflected prior to interacting with the normal standoff shock. In this case, the total pressure

decrease downstream of the normal standoff shock is less significant. At a higher P_e of 276 kPa in Figures 5-b, the incident shock waves have a smaller deflection angle thus preventing them to meet and reflect before interacting with the normal standoff shock. In this case, the total pressure decreases dramatically downstream of the normal standoff shock. The normal shock is formed due to a strong compression process when the flow traverses from subsonic to supersonic region. The strength of the normal shock is related to the extent of the compression. Regular reflection of the oblique shock from the axis may result in a static pressure rise large enough so that additional compression is not significant. In this case, the normal shock is weak. On the contrary, if the oblique shock directly interacts with the normal shock, significant compression is needed in order to establish the pressure necessary for the subsonic region and the normal shock is much stronger. The corresponding total pressure loss as flow crosses the normal shock is large if the shock strength is high, and small if low. For the case of small H (e.g., 1mm), the oblique shock always interacts with the standoff shock directly and therefore the total pressure after the standoff shock increases with the nozzle pressure and the through-hole mass flow rate always increases with the nozzle pressure.

The aforementioned explanation is confirmed by the axial variation of total pressure shown in Figure 6 for different nozzle pressures. The total pressure loss at higher nozzle pressures is so large that in fact the total pressure downstream of the standoff shock for a P_e of 276 kPa is less than that for a lower P_e of 258 kPa. The loss increases even further with P_e so that the total pressure downstream of the standoff shock for $P_e = 345$ kPa is nearly the same as that for P_e of 276 kPa.

Figures 7 shows the measured \dot{m}_h data for Group 2 experiments together with the simulation results. At P_e values of 125 kPa, \dot{m}_h is relatively unaltered with changes in H , indicating that the flow structure remains largely unchanged along the centerline. However, for a higher P_e value of 363 kPa, \dot{m}_h reduces continuously until a critical standoff distance, $H_{critical}$ of about 2.5mm is reached. At $H_{critical}$ a small increase in standoff distance results in a large jump in \dot{m}_h . Beyond this point \dot{m}_h continues to decrease with increasing H . The critical point is accompanied with strong shock noises heard during the experiments. The variation of computed \dot{m}_h with H is also shown in the figure. Once again the unique behavior of \dot{m}_h at a critical standoff distance is captured by the numerical simulations.

Figures 8-a and b show the contours of static pressure for $H = 2$ and 3.25mm, corresponding to two standoff distances before and after the jump in \dot{m}_h seen in Figure. In Figure 8-a ($H = 2.0$ mm), the incident shock interacts with the normal standoff shock directly. For low values of H , the through-hole mass flow rate decreases as the standoff distance increases as long as the incident shock directly meets the standoff shock. However, when the standoff distance reaches a point where the incident shock waves first meet at the centerline before they reflect and interact with the normal shock, the loss of total pressure is greatly reduced, which results in a jump of the through-hole mass flow rate. This sudden jump in mass flow rate at higher gas pressures is due to a change in shock structure associated with high shock strength.

In most laser machining cases, the nozzle standoff distance is chosen to be 0.5mm-1.5mm and thus the incident shock will always interact with the standoff shock directly. However, this study reveals that some favorable operating conditions do exist for large nozzle standoff distances within a certain range of the nozzle pressure. In those situations, the reflected shock is produced and interacts with the standoff shock, which has a higher total pressure downstream of the standoff shock. The nozzle pressure should be chosen to avoid direct contact between the incident shock and the standoff shock for large nozzle standoff distances. The low total pressure after the standoff shock is associated with fluctuations of the pressure gradient and shear stress inside the hole. Figure 9 and Figure 10 show the static pressure gradient and the shear force inside the hole for four different conditions. Large fluctuations in the pressure gradient and the shear force for $Pe = 276$ kPa and $H = 2$ mm corresponds to a characteristic behavior of that shown in Figure 5-b, where the incident shock has direct contact with the normal standoff shock. Since the pressure gradient and the shear force are two driving forces in melt removal, the fluctuation has detrimental effects on the removal capability of the gas jet, which often results in poorer cut quality.

5. Conclusions

The interaction of a gas jet with the workpiece in laser machining is investigated by systematically studying the influence of the processing parameters on the shock structure of the gas flow. The numerical simulation of a transonic, turbulent jet impinging on a plate (workpiece) with a hole concentric with the jet is presented, revealing the effects of gas pressure and nozzle standoff distance on shock structure. Experimental measurements of the mass flow rate through the hole under conditions corresponding to those of the simulation were carried out. Experimental data match the simulation results. Certain favorable operating conditions exist under which the oblique incident shock waves merges on the centerline and reflect before interacting with the normal standoff shock. In those cases, the total pressure loss across the standoff shock is less and a high total pressure remains at the machining front. The direct interaction of the incident waves and the normal standoff shock results in a large reduction of the total pressure across the standoff shock, conditions unfavorable to laser machining.

Acknowledgment

The work is supported by a National Science Foundation grant DMI-9500181.

References

- [1] Ivarson, A., *et al.* (1996), *J. of Laser Applications*, Vol. 8, pp. 191-196.
- [2] O'Neill, W. and Steen, W. M. (1995), *J. Phys. D: Appl. Phys.* Vol. 28, pp.12-18.
- [3] Chryssolouris, G., and Choi, W. C. (1989), *SPIE Vol. 1042 CO₂ Lasers and Applications*, pp. 86-96.
- [4] Bandt, A. D., and Settles, G. S. (1997), *J. of Laser Application*, Vol. 9, pp. 269-277.
- [5] LaRocca, A. V., *et al.* (1994), *SPIE Vol. 2207*, pp. 169-180.
- [6] O'Neill, W., *et al.* (1992), *Proc. ICALEO '92*, pp. 449-458.
- [7] Fieret, J., *et al.*, (1987), *SPIE Vol. 801 High Power Lasers*, pp. 243-250.
- [8] Addy, A. L. (1981), *AIAA Journal*, Vol. 19, pp. 121-122.
- [9] Gummer, J. H., and Hunt, B. L. (1971), *Aeronautical Quarterly*, Vol. 22, pp. 403.

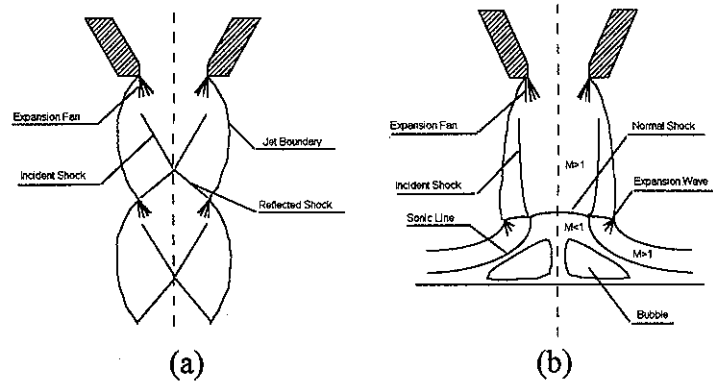


Figure 1 Schematic of underexpanded (a) free jet and (b) impinging jet

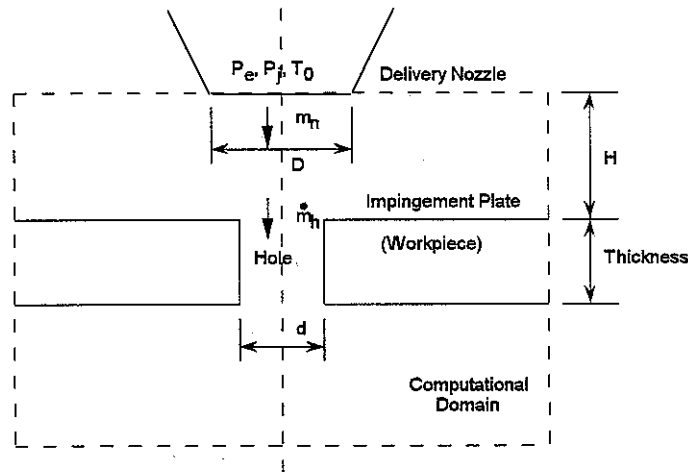


Figure 2 Schematic of computational domain for simulation

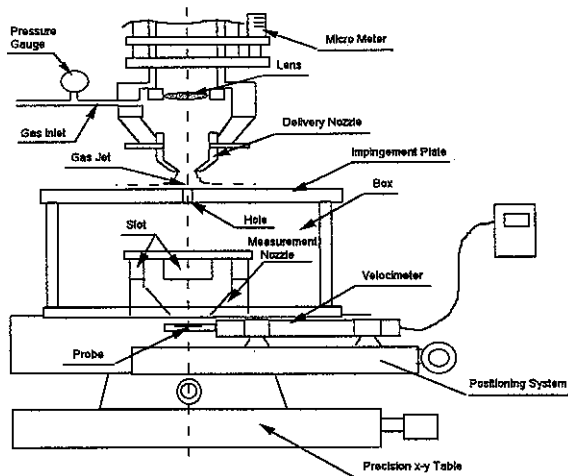


Figure 3 Schematic of experiment setup

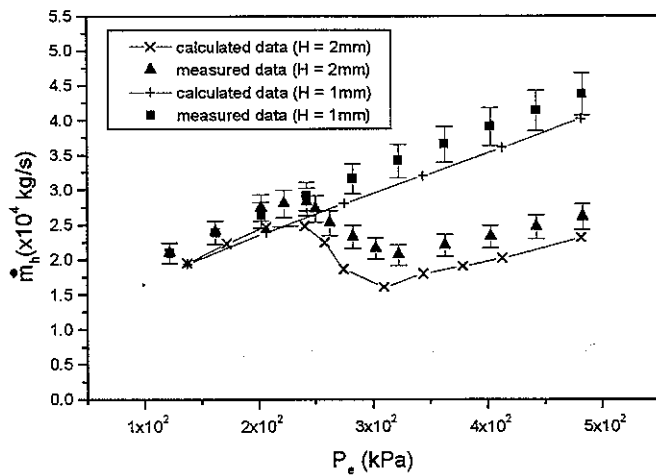


Figure 4. Computed and measured through-hole mass flow rate

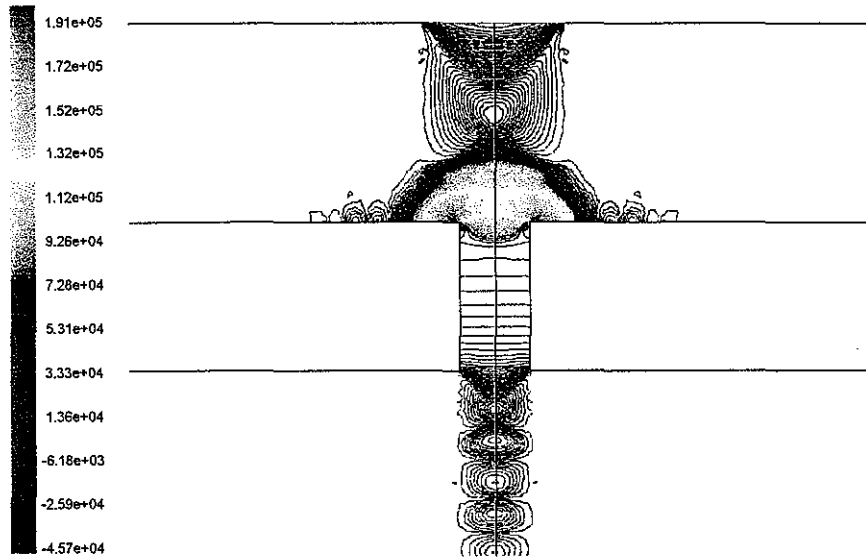


Figure 5-a Contour of static pressure (H=2mm) for $P_e = 207$ kPa

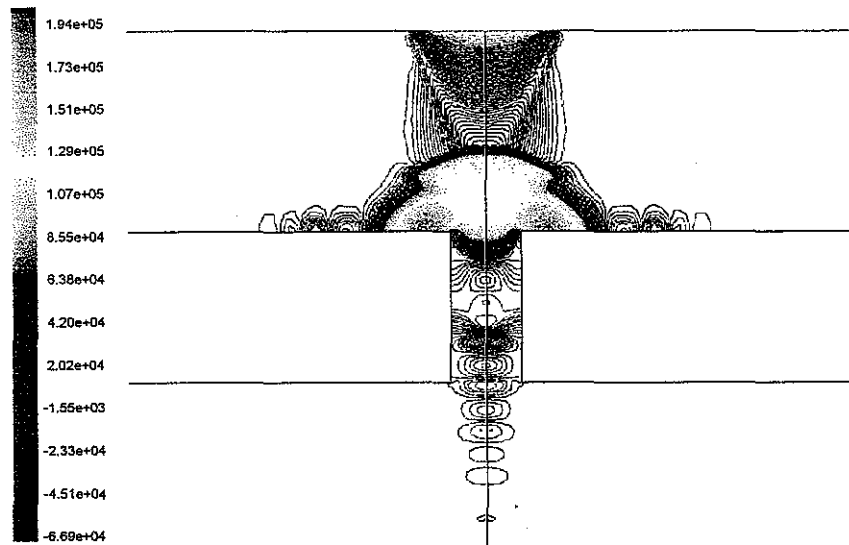


Figure 5-b Contour of static pressure (H=2mm) for $P_e = 276$ kPa

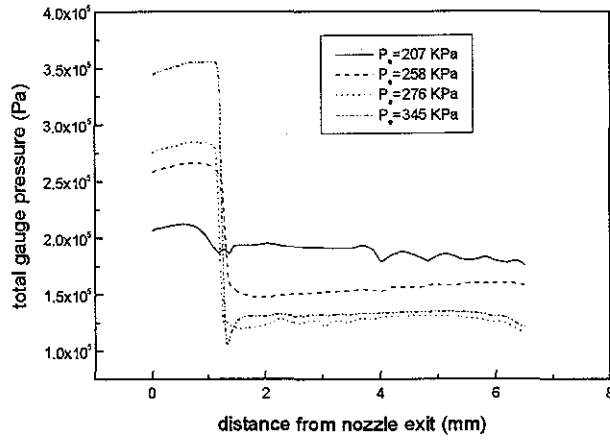


Figure 6. Computed variation of total pressure along the centerline for $H = 2.0\text{mm}$

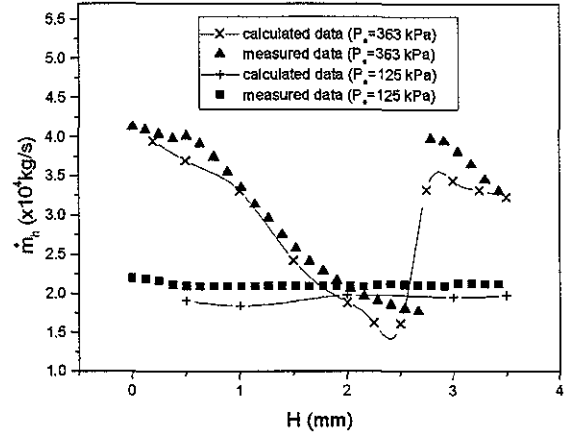


Figure 7. Computed and measured through hole mass flow rate

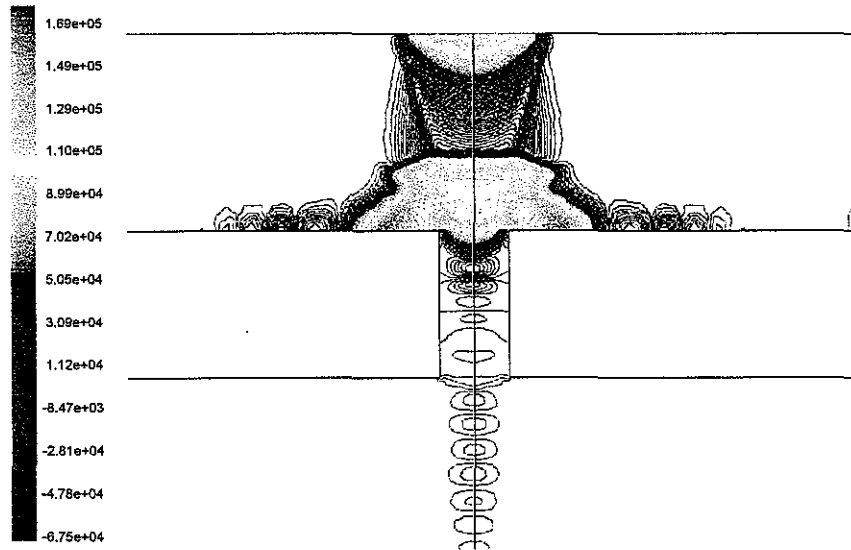


Figure 8-a Contour of static pressure ($P_0 = 363\text{ kPa}$) for $H = 2\text{mm}$

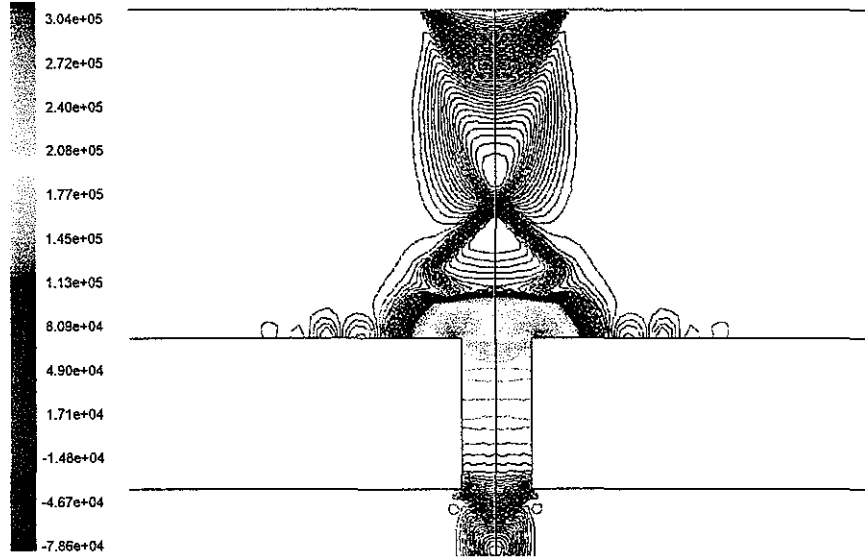


Figure 8-a Contour of static pressure ($P_e = 363 \text{ kPa}$) for $H = 3.25 \text{ mm}$

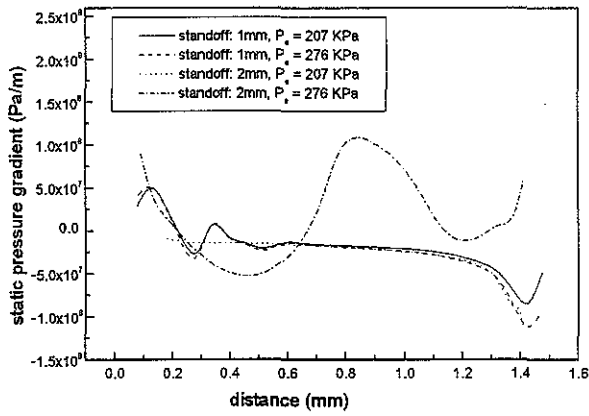


Figure 9. Static pressure gradient inside hole

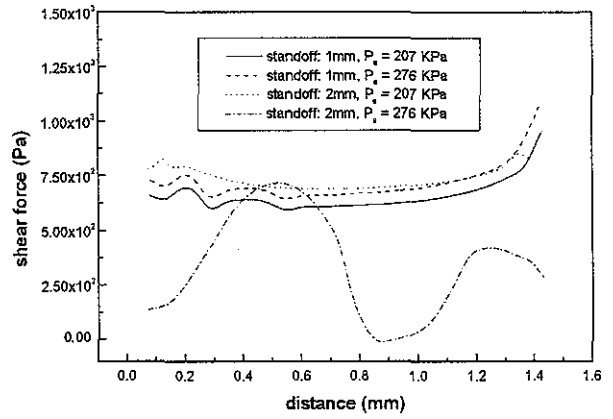


Figure 10. Shear force inside hole